Typhoon-Induced Microseisms around the South China Sea

Seongjun Park[1] and Tae-Kyung Hong[*1]

Abstract

Microseisms in frequencies of 0.05–0.5 Hz are a presentation of solid earth response to the ocean waves that are developed by atmospheric pressure change. The South China Sea provides a natural laboratory with a closed ocean environment to examine the influence of regional factors on microseism development as well as the nature of microseisms. The microseisms induced by typhoons crossing over the South China Sea are investigated. Typhoons are typical transient sources of varying strengths and locations. Primary microseisms develop nearly stationary in the northeastern South China Sea for most typhoons, suggesting effective environment for excitation of primary microseisms. Typhoon-induced secondary microseisms develop around the typhoon paths with time delays varying up to one day. Typhoon-induced microseism amplitudes are proportional to the ocean-wave amplitudes in the source regions, decaying with distance. Ocean waves develop following the typhoons for days. The dominant frequency of typhoon-induced microseisms increases with time due to the influence of dispersive ocean waves. The microseisms are affected by regional factors including crustal structures, coastal geometry, ocean depth, and ocean-bottom topography.

Cite this article as Park, S., and T.-K. Hong (2020). Typhoon-Induced Microseisms around the South China Sea, *Seismol. Res. Lett.* **91**, 3454–3468, doi: 10.1785/0220190310.

Introduction

The microseisms were first recognized in 1872 from an analysis of seismic record sections (Bertelli, 1872). Microseisms develop as a consequence of coupling among atmosphere, ocean, and solid earth. Ocean waves modulate the ocean-bottom pressure, inducing weak seismic energy that eventually develop as microseisms (Longuet-Higgins, 1950; Hasselmann, 1963; Haubrich and McCamy, 1969; Cessaro, 1994; Friedrich *et al.*, 1998; Bromirski and Duennebier, 2002; Shapiro *et al.*, 2006; Chevrot *et al.*, 2007; Yang and Ritzwoller, 2008; Landés *et al.*, 2010; Ardhuin *et al.*, 2011; Ebeling, 2012). The microseism development is dependent on the properties of ocean and atmosphere that are affected by regional factors including bathymetry, coastal geometry, ocean tide, and sea ice (Stehly *et al.*, 2006; Stutzmann *et al.*, 2006; Aster *et al.*, 2008; Ardhuin *et al.*, 2011; Gualtieri *et al.*, 2013; Davy *et al.*, 2014; Gal *et al.*, 2015).

Microseisms are divided into primary and secondary microseisms that are dominant in the frequencies of 0.05–0.5 Hz (Gutenberg, 1931; Longuet-Higgins, 1950; Donn and Blaik, 1952; Cessaro, 1994; Bromirski and Duennebier, 2002; Ardhuin *et al.*, 2012). The microseisms are composed of considerable surface-wave components with fractional body-wave components (Sutton and Barstow, 1990; Friedrich *et al.*, 1998; Gerstoft *et al.*, 2006; Zhang *et al.*, 2010). The ocean waves produce pressure on the ocean bottom, generating primary microseisms (Hasselmann, 1963; Bromirski, 2001; Chi *et al.*, 2010). The pressure induced by ocean waves decays exponentially with increasing ocean depth. Thus, the primary microseisms are effectively excited around coastal regions where ocean depths are shallow (Bromirski, 2001; Chi *et al.*, 2010). Also, the ocean-bottom topography plays additional role in the excitation of primary microseisms (Ardhuin *et al.*, 2015; Nishida, 2017).

The interference between ocean waves traveling in opposite directions (facing each other) produces the energy in the double frequencies of ocean waves, developing secondary microseisms (Longuet-Higgins, 1950; Hasselmann, 1963). The secondary microseisms develop in deep oceans as well as coastal regions (e.g., Bromirski, 2001). The secondary microseisms are generally stronger than the primary microseisms. The secondary microseisms are composed of long-period (0.08–0.2 Hz) and short-period (0.2–0.5 Hz) parts (Zhang *et al.*, 2010; Bromirski *et al.*, 2013).

Large storms including typhoons, cyclones, and hurricanes incorporate local and regional atmospheric circulation. Strong winds from large storms induce ocean waves that develop prominent microseisms (Gilmore, 1946; Longuet-Higgins, 1950; Webb, 1998; Gerstoft *et al.*, 2006; Chi *et al.*, 2010; Ardhuin *et al.*, 2011; Lee *et al.*, 2012). The origin, dimension, and strength of microseisms change with storm evolution. However, there are controversial observations including the

1. Department of Earth System Sciences, Yonsei University, Seoul, South Korea
*Corresponding author: tkhong@yonsei.ac.kr

TABLE 1
Information of Typhoons

Typhoon	Period (yyyy/mm/dd)*	Peak Central Pressure (hPa)†	Peak Wind Speed (m/s)†	Classification by JTWC
Son-Tinh	2012/10/23–2012/10/29	944	54	Typhoon
Jebi	2013/07/31–2013/08/03	978	31	Tropical storm
Wutip	2013/09/27–2013/10/01	948	51	Typhoon
Krosa	2013/10/29–2013/11/04	944	54	Typhoon
Haiyan	2013/11/03–2013/11/11	937	59	Super typhoon
Rammasun	2014/07/10–2014/07/19	918	72	Super typhoon
Kalmaegi	2014/09/11–2014/09/17	963	41	Typhoon
Mujigae	2015/10/01–2015/10/05	937	59	Typhoon

JTWC, Joint Typhoon Warning Center.
*Periods with central pressures equal to or lower than 1000 hPa.
†Peak strengths during passages over the South China Sea.

relationship between wind strength and induced microseisms (Gilmore, 1946; Tabulevich, 1971; Zhang *et al.*, 2010). Further, the roles of regional factors on the microseism development have been partially understood, despite various efforts (e.g., Hasselmann, 1963; Zhang *et al.*, 2010; Ardhuin *et al.*, 2011, 2015; Tian and Ritzwoller, 2015; Nishida, 2017).

The investigation of microseisms excited from apparent sources may enable us to understand the nature and excitation process of microseisms. Typhoons are transient sources to produce microseisms. The typhoon-induced microseisms may provide unique information on the coupling among atmosphere, ocean, and solid earth (Ardhuin *et al.*, 2011; Bromirski *et al.*, 2013). The South China Sea is a unique region with dense seismic stations and closed ocean environment that typhoons often pass over. We investigate the microseisms generated in the South China Sea during typhoon passing-over. We examine the characteristics of microseisms including amplitudes, frequency contents, and source locations. The nature of microseisms and the influence of regional factors on microseism development are investigated.

Data

We analyze microseisms induced by typhoons that passed over the South China Sea. We choose strong typhoons of which lifespans do not overlap one another. We consider typhoons with minimum central pressures less than 985 hPa. We collect the best-track information on the typhoons from the Joint Typhoon Warning Center (see Data and Resources; Table 1). The information includes the central locations of typhoons, central pressures, and peak wind speeds at every 6 hr.

We select eight typhoons including Son-Tinh in October 2012, Jebi in July 2013, Wutip in September 2013, Krosa in October 2013, Haiyan in November 2013, Rammasun in July 2014, Kalmaegi in September 2014, and Mujigae in October 2015 (Fig. 1). Typhoons Jebi and Wutip developed in the central South China Sea (Fig. 1). The other typhoons were originated from the western Pacific, passing over the Philippine to the South China Sea. Typhoon Rammasun was the strongest with the minimum central pressure of 925 hPa. Typhoon Jebi is the weakest, with the minimum central pressure of 985 hPa on the South China Sea. Typhoon Haiyan presented remarkable peak central pressures of 890 hPa during passage over the western Pacific. The typhoon strengths decrease, while the typhoons pass over the land.

We collect broadband seismic records during the typhoon periods from 12 stations around the South China Sea from Incorporated Research Institutions for Seismology (see Data and Resources; Fig. 1). The spatial distribution of stations displays good azimuthal coverage for the typhoon trajectories. The sampling rates are 20–100 Hz. We additionally collect earthquake information from a global earthquake catalog to avoid earthquake effects on microseism records (see Data and Resources).

We use the power spectral densities of ocean-wave heights that are calculated by a global wave forecasting model, WAVEWATCH III of National Oceanic and Atmospheric Administration (Tolman, 1991). This global ocean-wave model (WAVEWATCH III) is based on the surface wind data from the European Centre for Medium range Weather Forecasting (Ardhuin *et al.*, 2011). The global ocean-wave model is widely used as a reference model (e.g., Gerstoft *et al.*, 2006; Bromirski *et al.*, 2013; Ardhuin *et al.*, 2015). The power spectral density data and surface wind information are available from Institut Français de Recherche pour I'Exploitation de la Mer (see Data and Resources). The surface wind information is composed of wind direction and magnitude at every 3 hr. The power spectral density model is discretized by 0.5° in longitude and latitude.

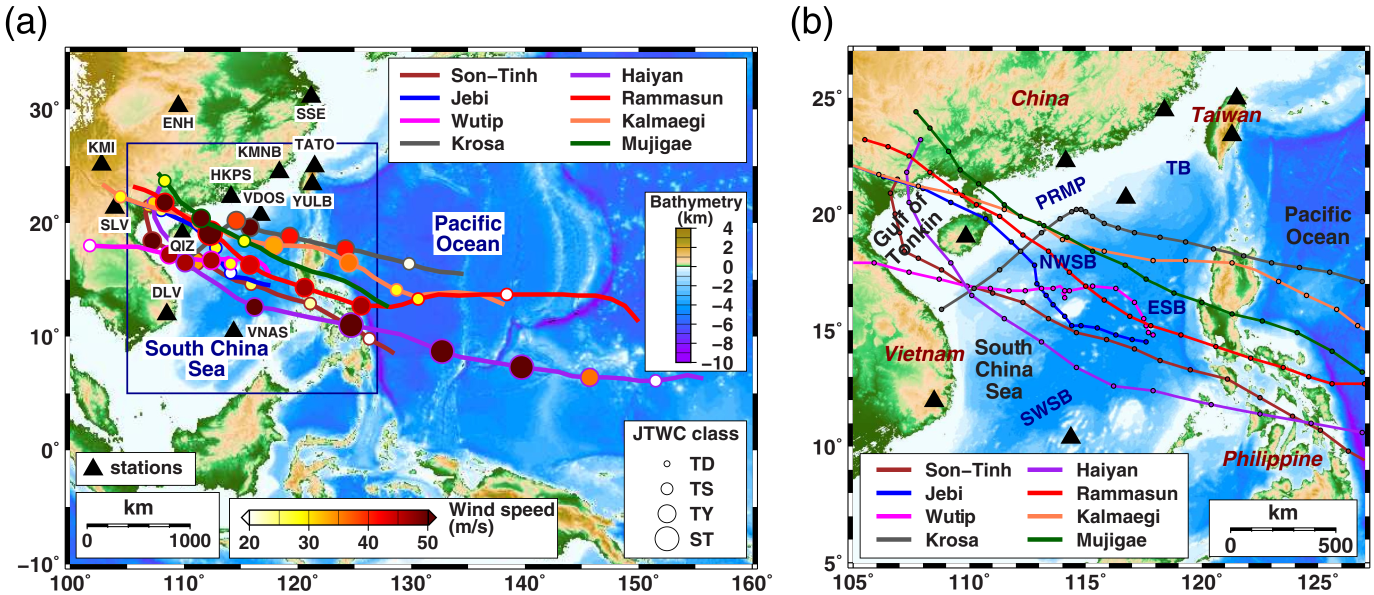

Figure 1. (a) Map of typhoon trajectories (solid lines) and regional seismic stations (triangles) around the South China Sea. Eight typhoons (Son-Tinh, Jebi, Wutip, Krosa, Haiyan, Rammasun, Kalmaegi, and Mujigae) are presented. The sizes of circles on trails present the typhoon classes assigned by the Joint Typhoon Warning Center (JTWC): tropical depression (TD), tropical storm (TS), typhoon (TY), and super typhoon (ST). The wind speeds are indicated. (b) Enlarged map around the South China Sea. Major geological structures are denoted: eastern South China Sea sub-basin (ESB), northwestern South China Sea sub-basin (NWSB), southwestern South China Sea sub-basin (SWSB), Tainan basin (TB), and Pearl River Mouth basin (PRMB). Typhoon locations at every 6 hr are marked with closed circles. The color version of this figure is available only in the electronic edition.

Methods

Seismic waves decay with distance. The attenuation of seismic energy from a point or small-size source satisfies (Atkinson and Mereu, 1992; Atkinson and Boore, 1995; Chiou and Youngs., 2008; Ford *et al.*, 2008; Bindi *et al.*, 2011):

$$\log A = W - \alpha \log r - \beta r, \quad (1)$$

in which A is the power spectral density in m^2/s, W is a constant for source strength, r is the distance in kilometers, and α and β are constants for geometrical spreading effect and inelastic attenuation. The source strength changes with typhoon evolution. Constants W, α, and β are determined from observed data set using a least-squares-fitting method with an assumption that the seismic energy decays uniformly with distance. Here, constant α is given by 1.0 for surface waves that spread cylindrically from the source.

A considerable energy of microseisms is composed of Rayleigh and Love waves (Sutton and Barstow, 1990; Friedrich *et al.*, 1998; Nishida *et al.*, 2008). The dominant composition of surface waves in microseisms enables us to use a surface-wave polarization analysis based on single stations (Tanimoto *et al.*, 2006; Schimmel *et al.*, 2011). The Rayleigh waves present a characteristic retrograde particle motion on the vertical–radial plane. On the other hand, the Love waves are strong in the transverse component. The phase difference of Rayleigh waves between vertical and radial components is $\pi/2$.

The horizontal displacement for azimuth θ at time t, $u_H(\theta, t)$, is given by

$$u_H(\theta, t) = \cos(\theta) u_N(t) + \sin(\theta) u_E(t), \quad (2)$$

in which $u_N(t)$ and $u_E(t)$ are ground displacements in north–south and east–west components at time t. The vertical displacement with a phase shift of $\pi/2$, u_Z^*, is given by

$$u_Z^*(t) = \int U_Z(f) \exp\left[i \left(2\pi f t + \frac{\pi}{2} \right) \right] df, \quad (3)$$

in which U_Z is the Fourier transform of vertical displacement (u_Z).

The phase correlation between u_H and u_Z^* for direction θ is estimated by

$$C(\theta) = \frac{\int_{t_1}^{t_2} u_Z^*(t) u_H(\theta - 180°, t) dt}{\sqrt{\int_{t_1}^{t_2} \{u_Z^*(t)\}^2 dt} \sqrt{\int_{t_1}^{t_2} \{u_H(\theta - 180°, t)\}^2 dt}}, \quad (4)$$

in which t_1 and t_2 are the start and end times of waveforms for comparison (Fig. 2). We determine the location of microseism sources using the polarization directions of Rayleigh waves in multiple stations (e.g., Cessaro, 1994; Yang and Ritzwoller, 2008; Tian and Ritzwoller, 2015). We stack the polarization directions of Rayleigh waves in stations by

$$B_i = \frac{1}{N} \sum_{j}^{N} C(\theta_{i,j}), \quad (5)$$

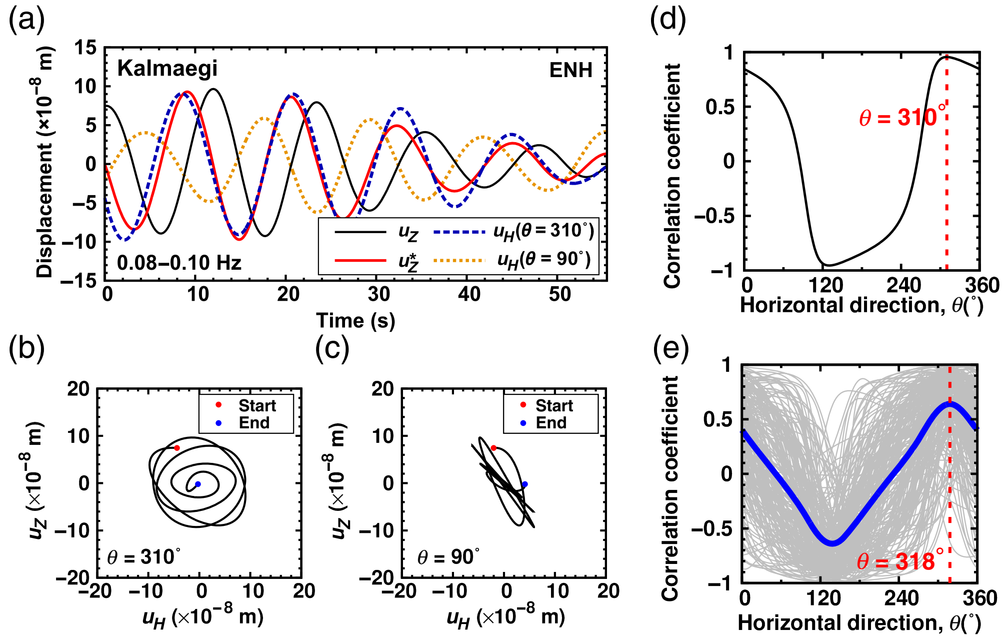

Figure 2. Determination of polarized orientation of Rayleigh-wave component in microseisms. (a) Comparison of microseism displacements between vertical (u_Z) and radial (u_H) components for radial directions of $\theta = 310°$ and 90°. Vertical waveforms phase-shifted by $\pi/2$ are presented (u_Z^*). High waveform correlations are observed between u_Z^* and u_H for $\theta = 310°$. (b) Particle motions on vertical planes for (b) $\theta = 310°$ and (c) 90°. Elliptical and retrograde particle motions are observed for $\theta = 310°$. (d) Variation of phase correlation between u_H and u_Z^* as a function of θ. Peak phase correlation is observed at $\theta = 310°$. (e) Phase correlation functions for 3 hr between u_H and u_Z^*. The average phase correlation function is marked with a thick solid line. The color version of this figure is available only in the electronic edition.

in which B_i is the stacked correlation coefficient at location i, N is the number of stations, and $\theta_{i,j}$ is the azimuthal direction from station j to location i.

Analysis

We analyze instrument-response-corrected velocity records in vertical component to investigate the typhoon-induced microseisms. We calculate the power spectral densities based on 30-minute-long record sections to examine the temporal changes in frequency contents of the microseisms (Fig. 3). The power spectral density represents the microseism strength. Transient seismic waves from earthquakes may interfere with the microseisms, producing vertical streaks in the spectrograms (Fig. 3). We exclude 3-hour-long records after major earthquakes with magnitudes greater than or equal to M_w 6.0 from microseism records in the analysis. Record sections for 1 hr after regional earthquakes of magnitudes $M_w \geq 5.0$ are removed in the analysis.

Continuous velocity records are segmented for moving time windows with 50% overlapping. The window sizes are set to be 10 times the central periods (the inverses of the central frequencies of the frequency bands). The segmented velocity records are converted into displacement waveforms and band-pass filtered using a cosine-tapered filter. The phase correlation functions are determined for the central half of the waveform segments.

The phase correlation functions are calculated for the frequency bands in which primary and secondary microseisms are dominant. We consider narrow frequency bands around the peak frequencies to avoid the apparent features associated with frequency-dependent energy modulation. We calculate the phase correlation function for azimuths θ at intervals of 1° (Fig. 2). Also, we assess the stacked correlation coefficients for every 3 hr, which enhances the stability of results.

Ambient Microseisms in Typhoon Absence

Ambient microseisms are composed of energy from various sources, including local wind fields, regional storms, and traveling swells (e.g., Cessaro and Chan, 1989; Bromirski and Duennebier, 2002; Ardhuin *et al.*, 2011; Tian and Ritzwoller, 2015). We examine the properties of ambient microseisms in the absence of typhoon. We investigate the ambient microseisms during winter (1 January 2014–6 January 2014) and summer (28 June 2014–3 July 2014) in the northern hemisphere.

The ambient microseisms present seasonal variations in strengths and frequencies (Fig. 3). We find primary microseisms with peak frequencies of 0.05–0.07 Hz in the winter and summer periods (Fig. 3). Secondary microseisms developed in frequencies around 0.13–0.17 Hz in the winter periods and 0.10–0.14 Hz in the summer periods. We observed inconsistent high-frequency energy that might be originated from local sources.

We determine the incidence directions of microseisms from the polarization orientation of Rayleigh waves in microseisms. We analyze the microseisms considering the dominant frequency bands. The primary microseisms in the winter are incident from northwest in back azimuths of 300°–360° (Fig. 3). On the other hand, the primary microseisms in the summer were originated in southwest in back azimuths of 190°–230°. According to the back-azimuth analysis, the ambient primary microseisms are originated from a far region with strong ocean waves.

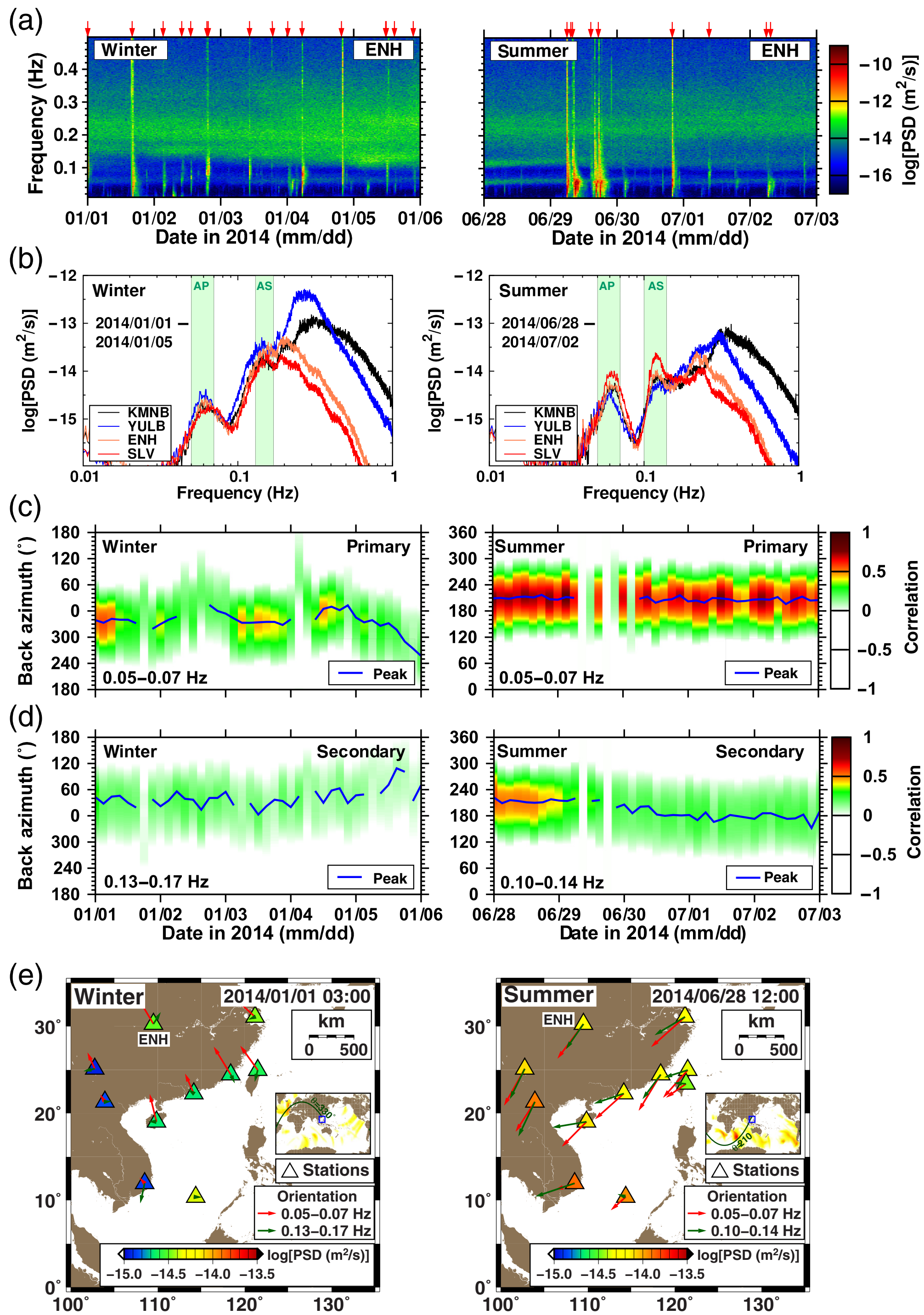

Figure 3. Properties of ambient microseisms in typhoon-absence periods in winter and summer. (a) Spectrograms of vertical velocity records at an inland station (ENH). Primary microseisms are dominant at frequencies of 0.05–0.07 Hz, and secondary microseisms at 0.10–0.14 Hz. Notable seismic waves from major earthquakes are indicated with arrows. (b) Average spectrums at common stations during the periods of typhoon absence. Ambient primary (AP) microseisms and ambient secondary (AS) microseisms are indicated. Spectrograms of (c) AP and (d) AS microseisms in the winter and summer periods. The back azimuths of peak correlations are marked with solid lines. The frequency bands are indicated. (e) Spatial variations in microseism orientations and amplitudes in the winter and summer. The directions to the microseism sources are marked (arrows on stations). The average power spectral densities (PSDs) of the primary microseisms are denoted. The global distributions of PSDs of ocean wavefield at 0.06 Hz are presented (insets). The color version of this figure is available only in the electronic edition.

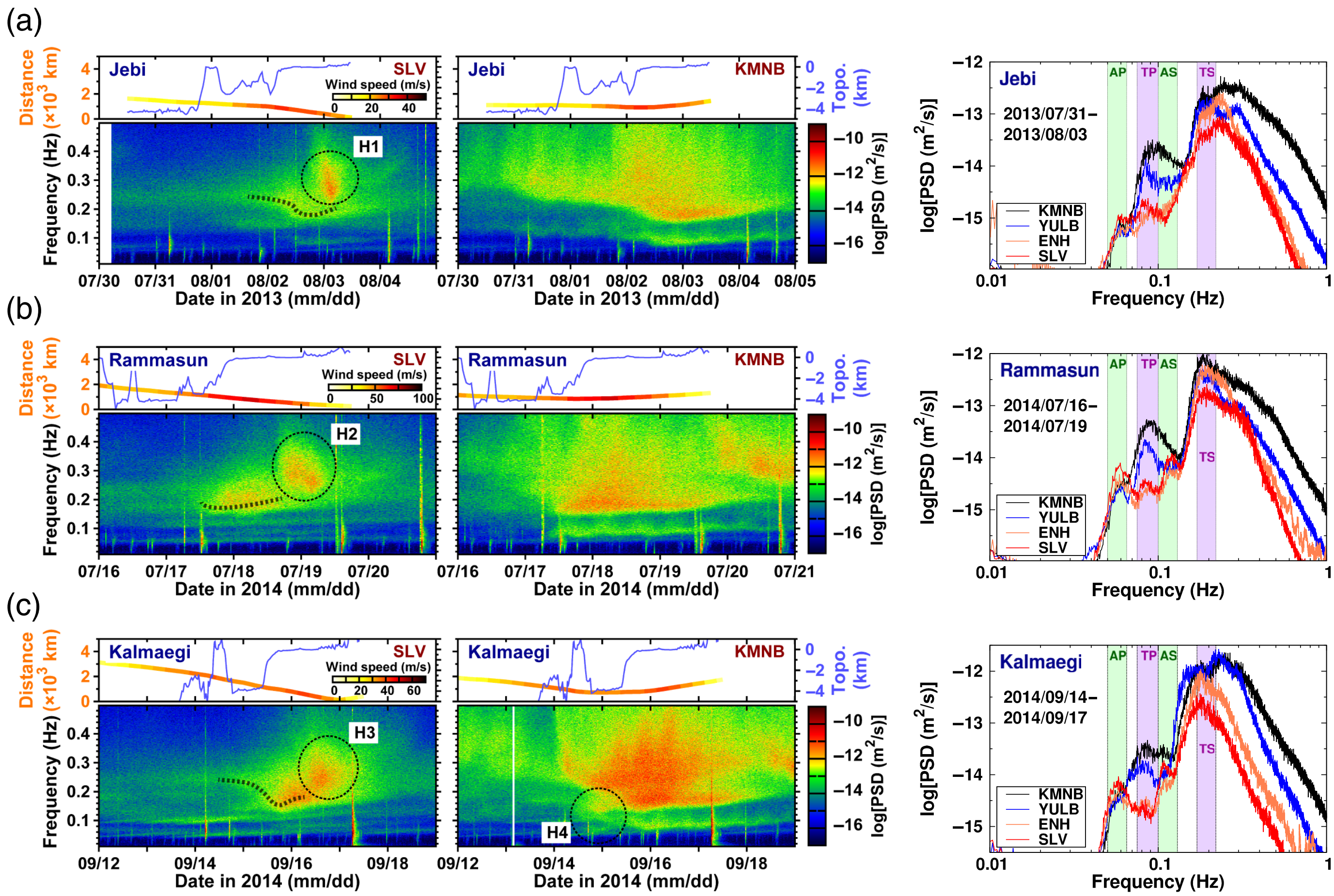

Figure 4. Spectral contents of microseisms during typhoon passage: Typhoons (a) Jebi, (b) Rammasun, and (c) Kalmaegi. (Left) Spectrograms at an inland station SLV and a coastal station KMNB. The typhoon–station distances (thick solid lines) and topography beneath typhoon centers (thin solid lines) are presented. The peak wind speeds of typhoons are denoted. The spectral contents change with time. The microseism strength increases with decreasing distance. The temporal changes in dominant frequencies are indicated (dotted lines). Typhoon-induced primary and secondary microseisms develop at lower and higher frequencies depending on the typhoon paths and station environments (H1, H2, H3, and H4). (Right) Average spectrum during typhoon periods. The typhoon-induced primary (TP) and secondary (TS) microseisms are marked along with the AP and AS microseisms. The color version of this figure is available only in the electronic edition.

The ambient secondary microseisms are weak due to discriminative attenuation of Rayleigh waves (Bromirski *et al.*, 2013; Nishida, 2017), causing unstable determination of secondary-microseism source locations. The back azimuths of the ambient secondary microseisms present similar directions to the ambient primary microseisms, in general (Fig. 3). The observation suggests that the dominant sources of primary and secondary microseisms may be located closely. The back-azimuth difference between the winter and summer periods suggests a seasonal variation in the ambient microseism origins.

It is noteworthy that ocean waves are generally weak in the South China Sea in the periods of typhoon absence. The microseisms rarely develop in the South China Sea during the periods of typhoon absence.

Typhoon-Induced Primary Microseisms

We analyze the seismic records around the South China Sea in typhoon periods to investigate the properties of typhoon-induced microseisms including strengths, frequency contents, and source locations (Fig. 4). The typhoon-induced microseisms are identified in the spectrograms (Fig. 4).

We observe that typhoon-induced microseisms are mixed with distant ambient microseisms. We observe abrupt increases in microseism amplitudes when typhoons are close to the stations (Fig. 4). We observe the prominent primary microseisms with peak frequencies of 0.07–0.12 Hz at most typhoons. The dominant frequency of primary microseisms increases mildly with time, which may be due to the dispersion of ocean waves (Bromirski, 2001; Ardhuin *et al.*, 2011).

The typhoon-induced microseisms are stronger in the coastal region of the northern South China Sea (e.g., station KMNB; Fig. 5). The primary microseisms are relatively weak

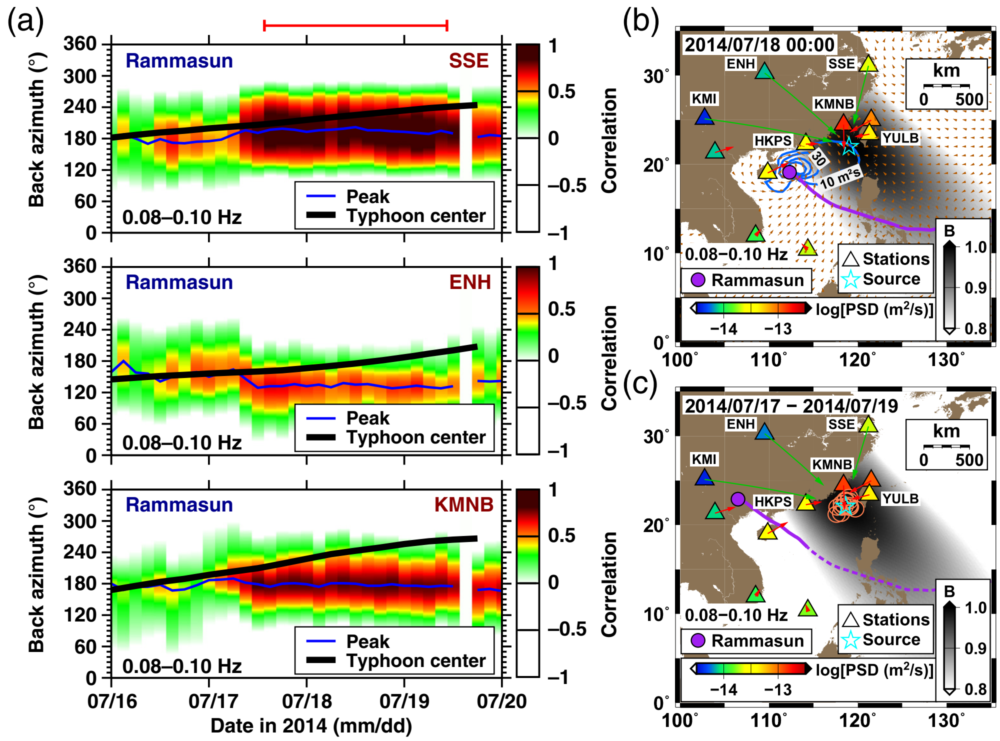

Figure 5. Determination of primary-microseism source locations during the passage of typhoon Rammasun. (a) Temporal changes in phase correlation functions for microseisms in frequencies of 0.08–0.10 Hz at stations. The back azimuth to typhoon center is presented (thick solid line). The back azimuths to primary-microseism sources (thin solid lines) are nearly stationary over time periods (solid horizontal bars on time axes). (b) Normalized stacked phase correlations (B) and inferred primary-microseism source location (star) in 12 a.m. 18 July 2014. The orientations of observed microseisms at stations are presented (arrows). The arrow lengths on stations present the phase correlations. The PSDs of ocean waves in 0.088 Hz are marked with contours. The surface wind fields over the oceanic regions are presented. (c) Stacked phase correlations for a period of 17 July 2014–19 July 2014. The peak locations of normalized phase correlations in every 3 hr are marked (open circles). The color version of this figure is available only in the electronic edition.

We compare the temporal variation of primary-microseism amplitudes with the ocean-wave amplitude model (Fig. 7). We find high correlation between the primary-microseism amplitudes and ocean-wave amplitudes around the determined primary-microseism source locations (location A in Fig. 7). Also, the active periods of the primary-microseism sources agree with the temporal variations in peak ocean-wave amplitudes (Figs. 6 and 7). The observation suggests that the source strength of primary microseisms is proportional to the ocean-wave amplitude (e.g., Hasselmann, 1963; Ardhuin *et al.*, 2015). The typhoon-induced ocean waves last for several days even after typhoon passing-over, developing the primary microseisms subsequently.

We determine the attenuation equation for power spectral densities of primary microseisms in vertical records (Fig. 8). We consider a reference source location in the northeastern South China Sea to calculate the distances to stations (location A in Fig. 8). The primary microseisms in the vertical records are dominated by Rayleigh waves. We, thus, set constant α for geometrical spreading effect in equation (1) to be 1. We find constant β for anelastic decay effect to be 2×10^{-4}–4×10^{-4} (Fig. 8). The theoretical primary-microseism attenuation curves reasonably represent the observed data points. The observation suggests that the microseism-inducing sources are nearly stationary in space. Also, it may be possible to estimate the microseism source strengths based on the observed microseism amplitudes using the attenuation equation (e.g., Hong *et al.*, 2019).

at inland regions (e.g., stations ENH and SLV). The Rayleigh-wave component develops stably in the typhoon-induced primary microseisms. We determine the horizontal incidence angle of the Rayleigh waves using a phase correlation function. The incidence directions of typhoon-induced primary microseisms are nearly constant while typhoons are active (Fig. 5). The observation suggests that the typhoon-induced primary microseisms are originated in constant locations (Fig. 5).

We determine the primary-microseism source locations using the stacked correlation functions (Figs. 5 and 6). We calculate the stacked correlation functions of seismic noise records in inland stations. The primary-microseism sources are located around the northeastern South China Sea, and rarely change with time (Fig. 5). The source locations of the typhoon-induced primary microseisms do not agree with the spatial distribution of ocean-wave amplitudes. The typhoon-induced primary microseisms developed consistently in the northeastern South China Sea.

We observed that strong typhoons such as Haiyan and Kalmaegi developed additional lower-frequency (0.06–0.08 Hz) primary microseisms outside the South China Sea, in the oceanic region off the northeastern Philippine islands (H4 in Fig. 4 and G in Fig. 9). The primary-microseism source location corresponds to a region of strong ocean waves. We also observe secondary microseisms associated with the lower-frequency primary microseisms (Fig. 9). The lower-

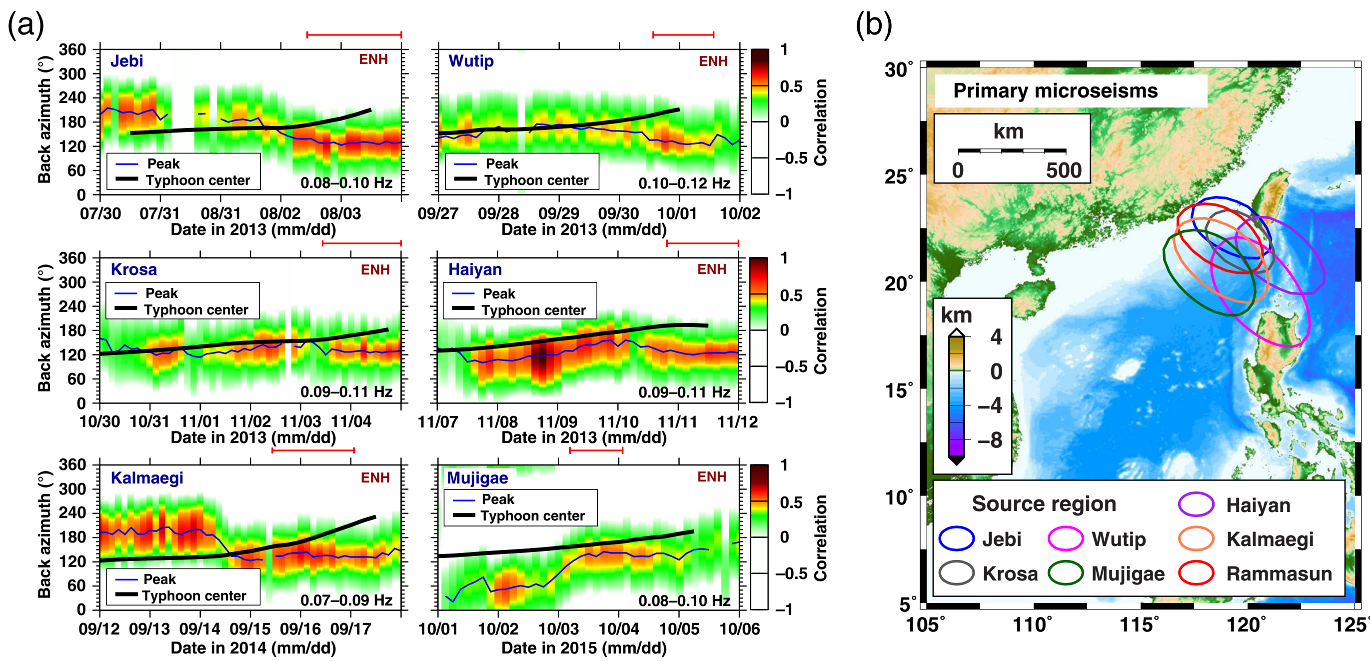

Figure 6. Comparison of primary-microseism origins for seven typhoons (Jebi, Wutip, Krosa, Haiyan, Rammasun, Kalmaegi, and Mujigae). (a) Temporal changes in phase correlation functions for primary microseisms at station ENH. The analyzed frequency bands are adjusted considering the frequency contents of primary microseisms. The time periods of stationary primary-microseism origins are indicated (bars on time axes). (b) Source locations of typhoon-induced primary microseisms. The areas of normalized stacked phase correlations larger than 0.99 are presented (ellipses). The color version of this figure is available only in the electronic edition.

frequency primary microseisms may be excited by long-period ocean waves developed by strong typhoons in the western Pacific.

Typhoon-Induced Secondary Microseisms

We observe typhoon-induced secondary microseisms in frequencies around 0.2 Hz. The amplitudes of typhoon-induced secondary microseisms gradually increase as typhoons approach to stations (Fig. 4). The strong typhoon-induced secondary microseisms last for several days after the passage of typhoons. The feature is associated with the ocean-wave evolution. We find that the typhoon-induced ocean waves last a few days after typhoon passage, developing the secondary microseisms subsequently (Fig. 7). The duration of microseism sources may vary by region-dependent environmental factors. The observations suggest that the typhoon-induced secondary-microseism sources may follow the typhoons, evolving with time (e.g., Gerstoft *et al.*, 2006; Zhang *et al.*, 2010).

This feature agrees with the secondary-microseism source locations inferred from the stacked correlation functions and Rayleigh-wave polarization directions (Fig. 10). Thus, the sources may be located in the oceans under and behind the typhoons, which agrees with the spatial variation of ocean-wave amplitudes (Fig. 10). The secondary microseisms develop effectively in the complex ocean wavefields around typhoons (e.g., Gerstoft *et al.*, 2008; Zhang *et al.*, 2010; Ardhuin *et al.*, 2011).

It is noteworthy that the microseism field around the coast is a mixture of dominant regional microseisms and locally induced microseisms (Zhang *et al.*, 2010). The polarization orientations of incoming microseisms are incoherent in costal stations (e.g., HKPS and YULB). Thus, the dominant regional microseisms are poorly resolved from the records in coastal stations (Fig. 10).

We find that the typhoon-induced secondary microseisms develop over a region around typhoon locations of one day before to current position (Figs. 10 and 11). The typhoon-induced secondary-microseism source locations are not stationary in space and evolve with time continuously. It is noteworthy that the features are similar to the observations of microbarom sources trailing the storms (Hetzer *et al.*, 2010; Stopa *et al.*, 2012; Blom *et al.*, 2014). The amplitudes of secondary microseisms decay fast with distance (Bromirski *et al.*, 2013; Nishida, 2017), causing difficulty to determine the source locations in far distances.

We find changes in dominant frequencies of typhoon-induced secondary microseisms, as the typhoons approach the coasts. We observe higher dominant frequencies in the typhoon-induced secondary microseisms when the ocean depths beneath the typhoons are shallower (e.g., Hasselmann, 1963; Ardhuin *et al.*, 2011; Fig. 4). The apparent changes in

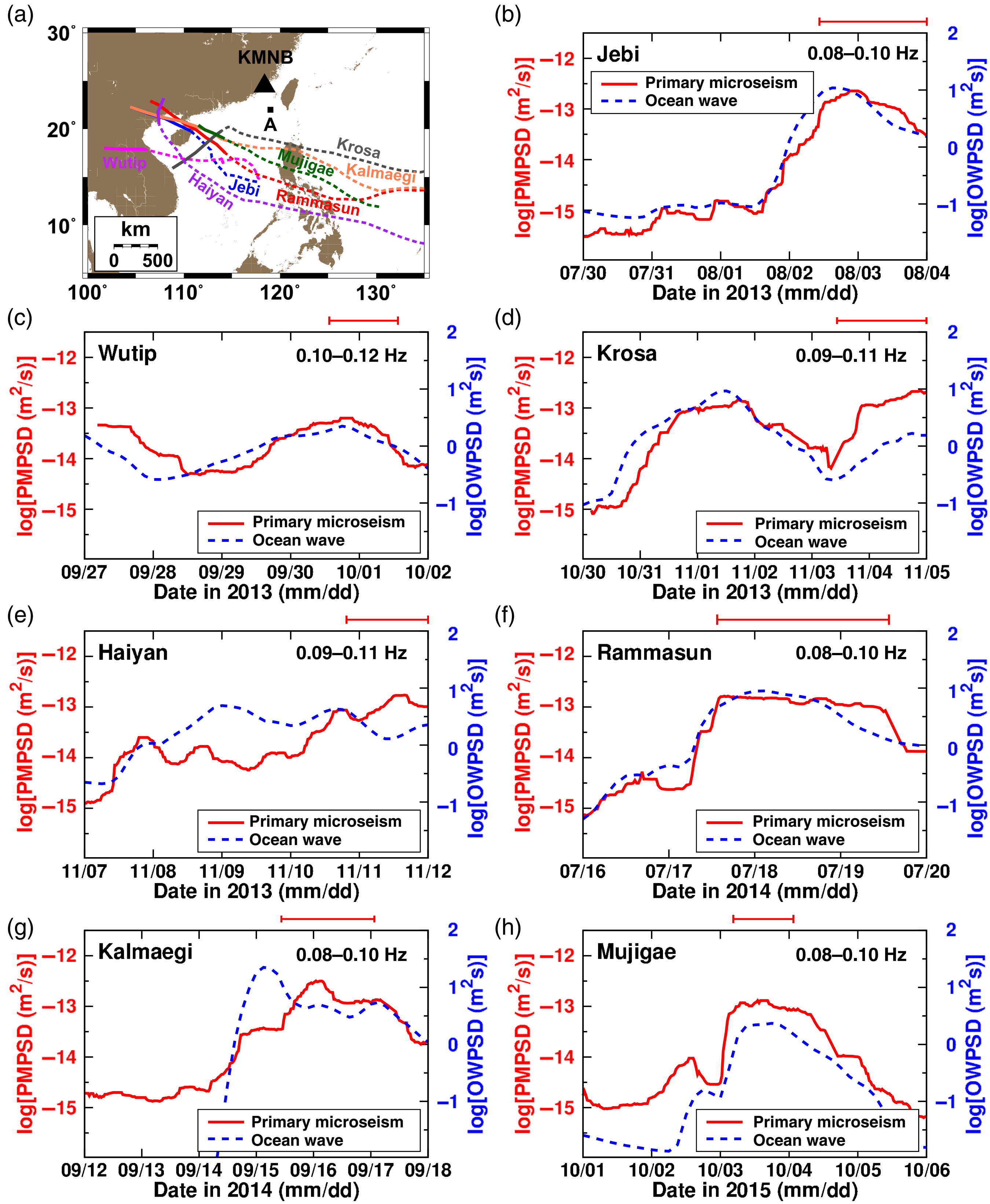

Figure 7. (a) Map of station (KMNB) and typhoon paths. Typhoon paths with stationary primary microseisms are marked by solid lines. Comparison between primary-microseism amplitudes and ocean-wave amplitudes for typhoons (b) Jebi, (c) Wutip, (d) Krosa, (e) Haiyan, (f) Rammasun, (g) Kalmaegi, and (h) Mujigae. The microseism amplitudes are correlated with ocean-wave amplitudes. The periods of stationary primary microseisms are marked (bars on time axes). OWPSD, ocean wave amplitude in power spectral density; PMPSD, primary microseism amplitude in power spectral density. The color version of this figure is available only in the electronic edition.

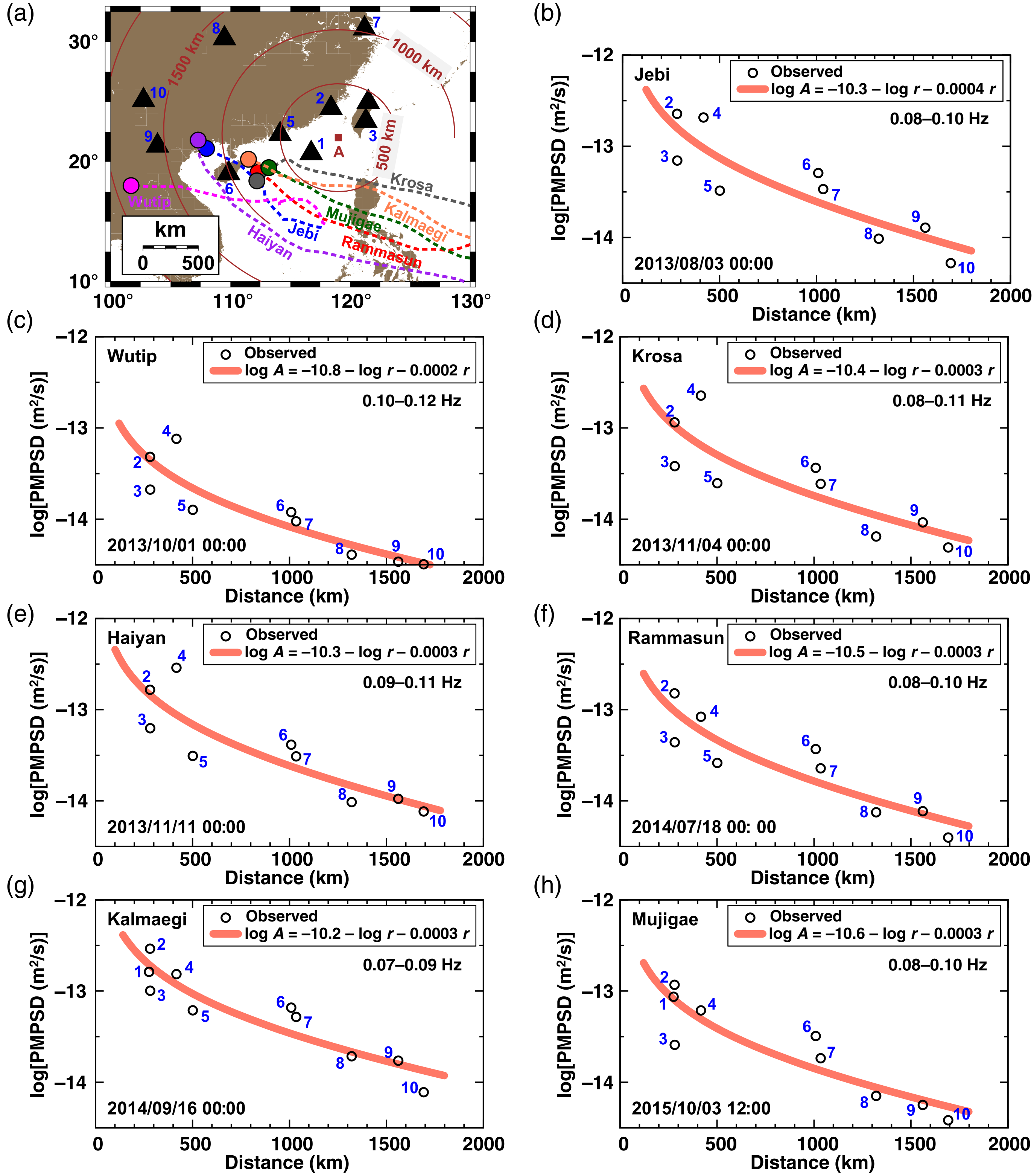

Figure 8. Attenuation of primary-microseism amplitudes as a function of distance. (a) Map of stations (triangles), typhoon locations (dashed lines), and primary-microseism source location (A). The stations are numbered in the order of distances to location A. The primary-microseism amplitudes for typhoons (b) Jebi, (c) Wutip, (d) Krosa, (e) Haiyan, (f) Rammasun, (g) Kalmaegi, and (h) Mujigae. The primary-microseism amplitude attenuates with distance. Best-fit curves are presented with solid lines. The color version of this figure is available only in the electronic edition.

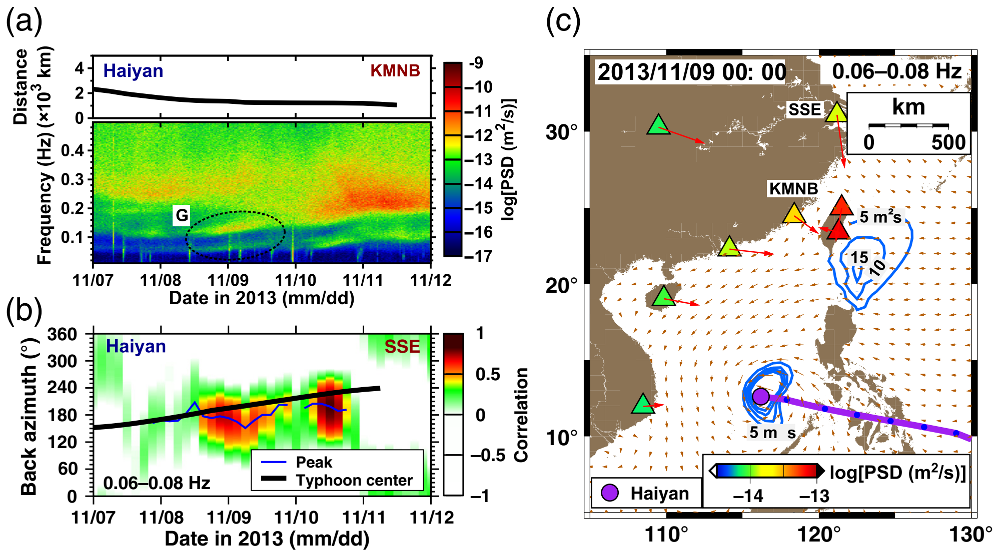

Figure 9. Low-frequency microseism excitation during passage of typhoon Haiyan. (a) Spectrogram of seismic records at station KMNB. Primary microseisms in frequencies of 0.06–0.08 Hz and secondary microseisms in 0.12–0.16 Hz are observed (G). (b) Temporal changes in phase correlation functions for primary microseisms at station SSE. (c) Directions to primary-microseism sources and ocean-wave amplitudes. The spatial distribution of PSDs of ocean waves at frequency of 0.073 Hz are presented (contours). The surface wind fields over the oceanic regions are denoted (arrows). The low-frequency primary microseisms originate in the oceanic region off the northeastern Philippine islands. The color version of this figure is available only in the electronic edition.

frequency contents are partly associated with the influence of dispersive ocean swells (Cathles *et al.*, 2009; Ardhuin *et al.*, 2011). The temporally varying typhoon strength may control the ocean-wave frequencies (Stewart, 2008). The dominant frequency of secondary microseisms decreases when the wind speed increases (Fig. 4).

A distance change between source and station causes a frequency-content change due to discriminative frequency-dependent attenuation. We also find that secondary microseisms with peak frequencies of 0.25–0.35 Hz develop when typhoons pass over a small oceanic region, Gulf of Tonkin (H1-3 in Fig. 4). The observation suggests that the oceanic environment such as bathymetry and geographical geometry controls the frequency contents of secondary microseisms.

Typhoon-Induced Microseism Excitation

The ocean waves rise gradually when the typhoons pass over the South China Sea. The typhoon-induced primary microseisms develop over time as the ocean-wave amplitude increases (Fig. 7). The observed typhoon-induced primary-microseism amplitudes are correlated with ocean-wave amplitudes in the northern South China Sea. The primary-microseism amplitude reaches the peak in a few days after the typhoon passage over the South China Sea (Figs. 1, 5, and 6). The typhoon-induced ocean waves produce the primary microseisms continuously. We find that the typhoon-induced primary-microseism sources for most typhoons are located nearly stationary around Tainan basin in the northeastern South China Sea. The source region of dominant primary microseisms is poorly resolved from the records in coastal stations due to the influence of heterogeneous local primary microseisms that are effective around coastal regions (Fig. 5).

The northeastern South China Sea presents a shallow ocean depth and characteristic ocean-bottom topography that are effective for primary-microseism excitation. Tainan basin has thick sedimentary layers, which may be effective for excitation of microseism energy for oceanic pressure (Li *et al.*, 2008; Deng *et al.*, 2013). It is noteworthy that low-velocity structures are present in the crust and upper mantle beneath Tainan basin (Wu *et al.*, 2004; Tang and Zheng, 2013; Li *et al.*, 2019). Low-velocity media effectively amplify the seismic waves (Hong, 2010; Hong and Lee, 2012; Jo and Hong, 2013). The low-velocity structures in the crust and mantle beneath Tainan basin may be effective to develop coherent and stationary microseisms.

The thickness of low-velocity layer controls the fundamental resonance frequency (Hong, 2014). The thickness of low-velocity zone may affect the strength and frequency content of the microseisms. The coastal geometry and environment affect the ocean-wave amplitudes due to focusing and defocusing effect in wave propagation, which may play additional role in microseism development (Hasselmann, 1963; Ardhuin *et al.*, 2015). The stationary primary-microseism sources suggest that the primary microseisms develop exclusively in the most favorable environment depending on the ocean depth, ocean-bottom topography, coastal geography, and geological structure (e.g., Hasselmann, 1963).

The typhoon-induced secondary-microseism sources are located in the oceanic regions below and behind typhoons (Figs. 10 and 11). We observe the secondary-microseism sources around the regions with large ocean-wave amplitudes (Fig. 10). The observation suggests that typhoons contribute to develop secondary microseisms with some time delays. The time delays appear to increase with distance from typhoon to coasts. The time delay may suggest the time required for stable development of ocean waves. The ocean waves are reflected in the coasts. The reflected ocean waves may interfere with incoming ocean waves, exciting the secondary microseisms. The ocean-wave interference may be particularly effective in oceanic regions near the coasts. The shallow ocean depths near the coasts may enhance the development of secondary microseisms.

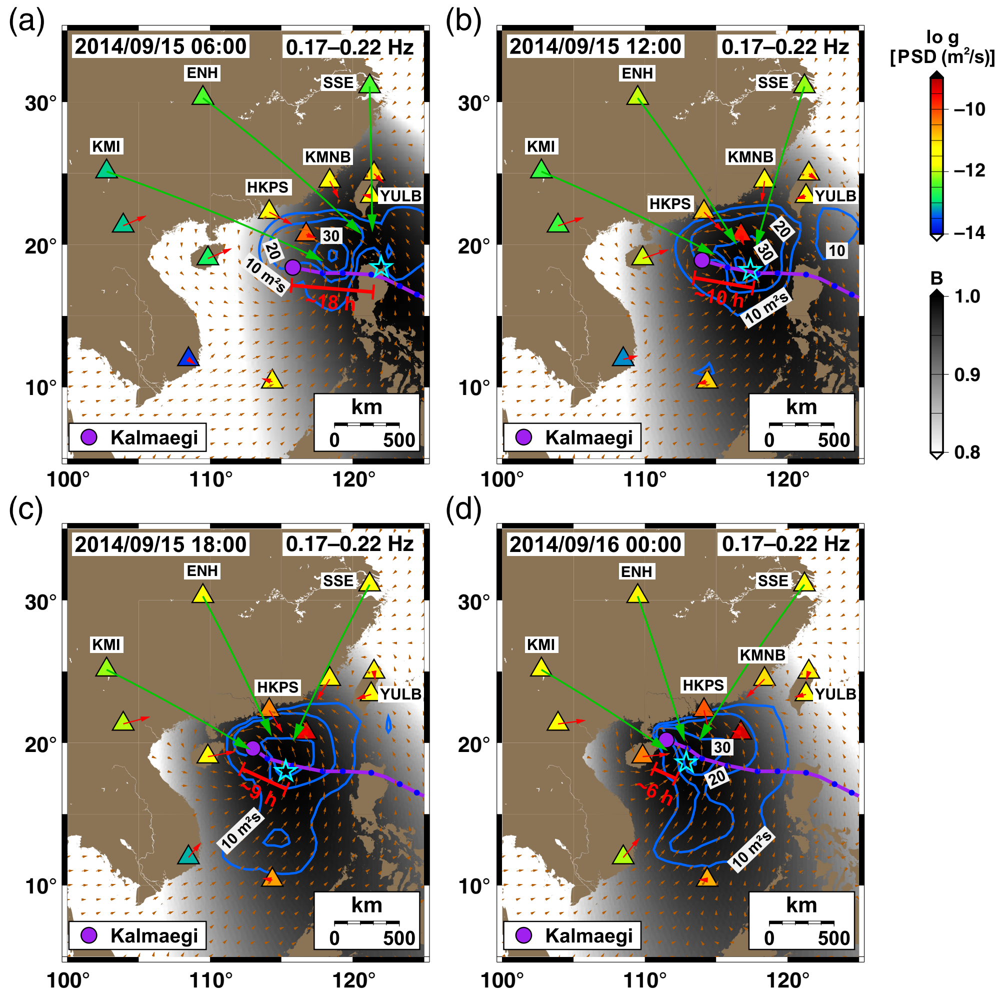

Figure 10. Source locations of secondary microseisms in 0.17–0.22 Hz during passage of typhoon Kalmaegi in 15 September 2014 at (a) 06:00, (b) 12:00, (c) 18:00, and (d) 24:00. The orientations of secondary microseisms at stations are indicated as arrows. The distributions of normalized stacked phase correlations (*B*) are presented with the locations of peak correlations (stars). The PSDs of ocean waves at 0.106 Hz are presented (contours). The secondary-microseism sources trail the typhoons. The time delays are annotated. The surface wind fields over the oceanic regions are denoted (arrows). The color version of this figure is available only in the electronic edition.

Discussion and Conclusions

We investigated the properties of typhoon-induced microseisms around the South China Sea. We compared the properties of typhoon-induced microseisms with those of ambient microseisms. The ambient microseisms are excited by long-period ocean waves (e.g., Bromirski and Duennebier, 2002; Tian and Ritzwoller, 2015). The ambient microseisms originate far away from the South China Sea. High-frequency ambient microseisms attenuate fast with distance. Thus, the microseism field is dominated by typhoon-induced microseisms, when typhoons pass over the South China Sea.

The dominant frequencies of typhoon-induced primary and secondary microseisms are 0.07–0.12 Hz and 0.17–0.22 Hz, which are higher than those of ambient microseisms. The difference in frequency contents between ambient microseisms and typhoon-induced microseisms appears to be associated with the differences in microseism source properties and source–station distances.

The typhoon-induced microseisms were composed of considerable amounts of surface waves and fractional body waves. We utilized the polarization of Rayleigh waves in typhoon-induced microseisms to determine the microseism source locations. The typhoon-induced primary microseisms were developed consistently in the northeastern South China Sea for different typhoons. The primary-microseism source locations were stationary during typhoon periods. The observation suggests that primary microseisms originate dominantly at certain places in favorable environment. The development of typhoon-induced primary microseisms may be controlled by local and reginal environment. In particular, low-velocity media beneath ocean bottom may be effective for excitation of strong and coherent primary microseisms, which may be consistent with the global origins of primary microseisms (Gerstoft and Tanimoto, 2007; Landés *et al.*, 2010; Schimmel *et al.*, 2011).

The typhoon-induced primary-microseism amplitudes are correlated with ocean-wave amplitudes around the northeastern South China Sea. The ocean waves in the South China Sea rise while typhoons are active, developing the microseisms. The features suggest that the microseisms

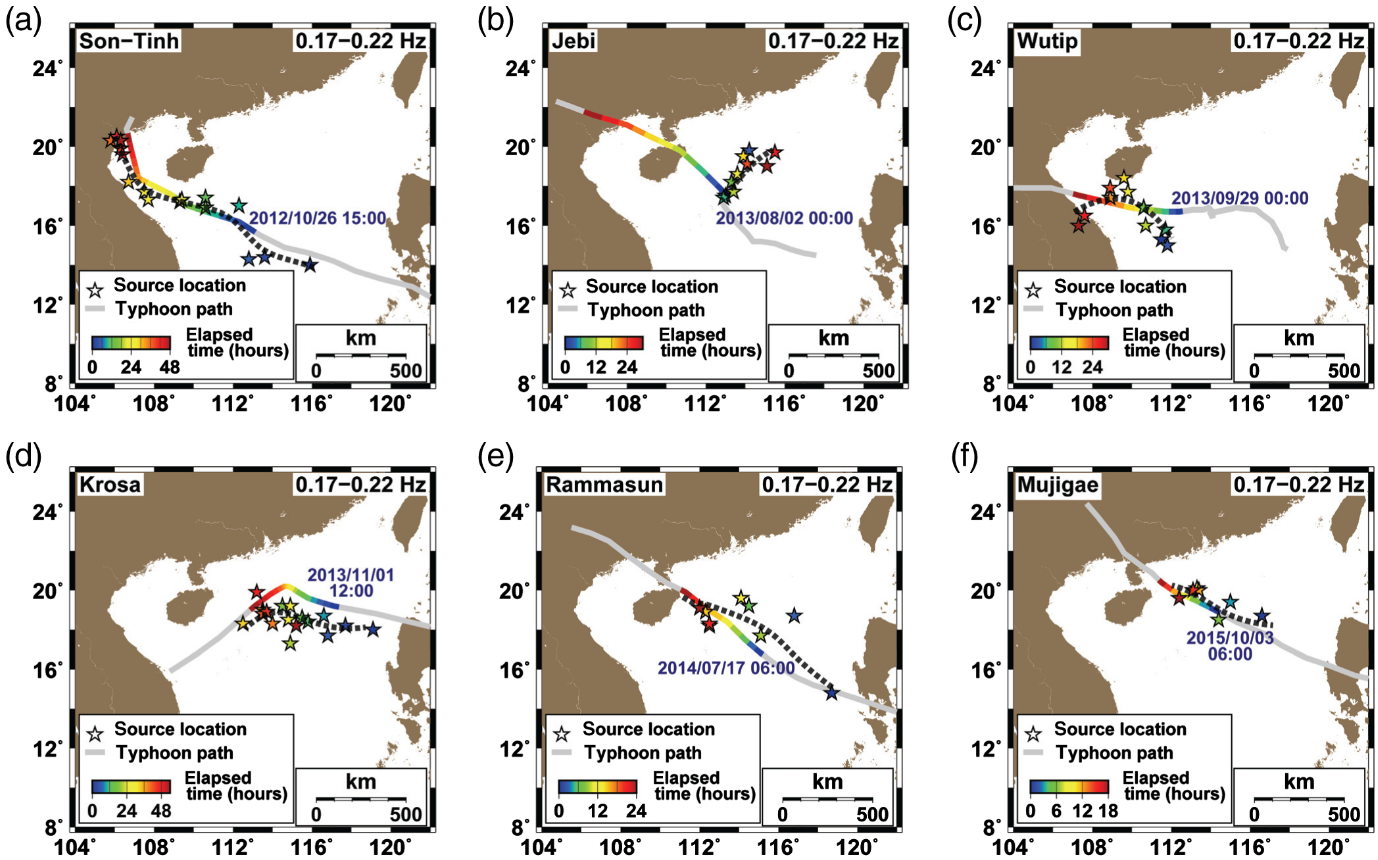

Figure 11. Temporal changes in secondary-microseism source locations for typhoons (a) Son-Tinh, (b) Jebi, (c) Wutip, (d) Krosa, (e) Rammasun, and (f) Mujigae. The secondary-microseism source locations are marked (stars). The trajectories of secondary-microseism source locations are marked (dotted-line areas). The secondary-microseism sources are located behind the typhoons. The time delays generally decrease, as typhoons approach to coasts. The color version of this figure is available only in the electronic edition.

may be used for monitoring of ocean waves. The apparent frequency increase in the typhoon-induced primary microseisms may be associated with ocean-wave dispersion (e.g., Friedrich *et al.*, 1998; Bromirski *et al.*, 2005; Schimmel *et al.*, 2011).

The observed amplitude of typhoon-induced secondary microseisms decreases with distance from station to typhoon. The observation suggests that the typhoon-induced secondary-microseism sources may be placed around typhoons. The frequency content of typhoon-induced secondary microseisms apparently changes with typhoon location. We observed lower-frequency contents for typhoons over a large open ocean and higher-frequency contents for those over a small closed sea (Gulf of Tonkin). The ocean depth, ocean size, and typhoon-evolving history (track, path, and central pressure) appear to control the frequency contents of microseisms (e.g., Hasselmann, 1963; Bromirski *et al.*, 2005; Chevrot *et al.*, 2007; Zhang *et al.*, 2010).

The typhoon-induced secondary microseisms develop in oceanic regions, trailing typhoons (Chi *et al.*, 2010; Ardhuin *et al.*, 2011). Our results show that the source locations of typhoon-induced secondary microseisms coincide with the regions of strong ocean waves behind the typhoons (Fig. 10). The interaction between the atmosphere and ocean may take up to a couple of days to build stable ocean waves. The time delay for the excitation of microseisms increases with distance between the typhoon and the coast. The time delays are large for typhoons over deep open oceans, whereas they are small for typhoons near the coasts. These observations suggest that environment factors including coastal geometry, ocean depth and ocean size, and geological structure play a primary role in the development of microseisms.

Data and Resources

The information on typhoons was collected from the Joint Typhoon Warning Center (https://www.metoc.navy.mil/jtwc/jtwc.html, last accessed in September 2019). The seismic waveforms were collected from the Incorporated Research Institutions for Seismology (http://ds.iris.edu/ds/, last accessed in September 2019). The global earthquake catalog was obtained from the U.S. Geological Survey (https://earthquake.usgs.gov/, last accessed in September 2019). We collected the power spectral densities of ocean-wavefield model and the surface wind information of the European Centre for Medium Range Weather Forecasting (ECMWF) from Institut Français de Recherche pour l'Exploitation de la Mer (Ifremer) (ftp://ftp.ifremer.fr, last accessed in April 2020).

Acknowledgments

Seongjun Park is grateful to Kiwamu Nishida for valuable discussion on microseisms. The authors thank Allison Bent (Editor-in-Chief), Pieter Smets, and an anonymous reviewer for fruitful review comments. This work was supported by the Korea Meteorological Administration Research and Development Program under Grant KMI2018-02910. In addition, this research was partly supported by National Research Foundation of Korea (NRF-2017R1A6A1 A07015374 and NRF-2018R1D1A1A09083446).

References

Ardhuin, F., A. Balanche, E. Stutzmann, and M. Obrebski (2012). From seismic noise to ocean wave parameters: General methods and validation, *J. Geophys. Res.* **117,** no. C05002, doi: 10.1029/2011JC007449.

Ardhuin, F., L. Gualtiery, and E. Stutzmann (2015). How ocean waves rock the Earth: Two mechanisms explain microseisms with periods 3 to 300 s, *Geophys. Res. Lett.* **42,** 765–772, doi: 10.1002/2014GL062782.

Ardhuin, F., E. Stutzmann, M. Schimmel, and A. Mangeney (2011). Ocean wave sources of seismic noise, *J. Geophys. Res.* **116,** no. C09004, doi: 10.1029/2011JC006952.

Aster, C., D. E. AcNamara, and P. D. Bromirski (2008). Multidecadal climate-induced variability in microseisms, *Seismol. Res. Lett.* **79,** 194–202, doi: 10.1785/gssrl.79.2.194.

Atkinson, G. M., and D. M. Boore (1995). Ground-motion relations for eastern North America, *Bull. Seismol. Soc. Am.* **85,** 17–30.

Atkinson, G. M., and R. F. Mereu (1992). The shape of ground motion attenuation curves in southeastern Canada, *Bull. Seismol. Soc. Am.* **82,** 2014–2031.

Bertelli, T. (1872). Osservazioni sui piccoli movimenti dei pendoli in relazione ad alcuni fenomeni meteorologiche, *Bull. Meteorol. Dell'Osservatorio Del Collegio Romano* **9,** 10 (in Italian).

Bindi, D., F. Pacor, L. Luzi, R. Puglia, M. Massa, G. Ameri, and R. Paolucci (2011). Ground motion prediction equations derived from the Italian strong motion database, *Bull. Earthq. Eng.* **9,** 1899–1920, doi: 10.1007/s10518-011-9313-z.

Blom, P., R. Waxler, W. G. Frazier, and C. Talmadge (2014). Observations of the refraction of microbaroms generated by large maritime storms by the wind field of the generating strom, *J. Geophys. Res.* **119,** 7179–7192, doi: 10.1002/2014JD021795.

Bromirski, P. D. (2001). Vibrations from the "Perfect Storm", *Geochem. Geophys. Geosys.* **2**, doi: 10.1029/2000GC000119.

Bromirski, P. D., and F. K. Duennebier (2002). The near-coastal microseism spectrum: Spatial and temporal wave climate relationship, *J. Geophys. Res.* **107,** 2166, doi: 10.1029/2001JB000265.

Bromirski, P. D., F. K. Duennebier, and R. A. Stephen (2005). Mid-ocean microseisms, *Geochem. Geophys. Geosys.* **6,** no. Q04009, doi: 10.1029/2004GC000768.

Bromirski, P. D., R. A. Stephen, and P. Gerstoft (2013). Are deep-ocean-generated surface-wave microseisms observed on land? *J. Geophys. Res.* **118,** 3610–3629, doi: 10.1002/jgrb.50268.

Cathles, L. M., E. A. Okal, and D. R. MacAyeal (2009). Seismic observations of sea swell on the floating Ross Ice Shelf, Antarctica, *J. Geophys. Res.* **114,** no. F02015, doi: 10.1029/2007JF000934.

Cessaro, R. K. (1994). Sources of primary and secondary microseisms, *Bull. Seismol. Soc. Am.* **81,** 142–148.

Cessaro, R. K., and W. W. Chan (1989). Wide-angle triangulation array study of simultaneous primary microseism sources, *J. Geophys. Res.* **94,** 15,555–15,563, doi: 10.1029/JB094iB11p15555.

Chevrot, S., M. Sylvander, S. Benahmed, C. Ponsolles, J. M. Lefevre, and D. Paradis (2007). Source locations of secondary microseisms in western Europe: Evidence for both coastal and pelagic sources, *J. Geophys. Res.* **112,** no. B11301, doi: 10.1029/2007JB005059.

Chi, W. C., W. J. Chen, B. Y. Kuo, and D. Dolenc (2010). Seismic monitoring of western Pacific typhoons, *Mar. Geophys. Res.* **31,** 239–251, doi: 10.1007/s11001-010-9105-x.

Chiou, B. J., and R. R. Youngs (2008). An NGA model for the average horizontal component of peak ground motion and response spectra, *Earthq. Spectra* **24,** 173–215, doi: 10.1193/1.2894832.

Davy, C., G. Barruol, F. R. Fontaine, K. Sigloch, and E. Stutzmann (2014). Tracking major storms from microseismic and hydroacoustic observations on the seafloor, *Geophys. Res. Lett.* **41,** 8825–8831, doi: 10.1002/2014GL062319.

Deng, J. M, T. K. Wang, B. J. Yang, C. S. Lee, C. S. Liu, and S. C. Chen (2013). Crustal velocity structure off SW Taiwan in the northernmost South China sea imaged from TAIGER OBS and MCS data, *Mar. Geophys. Res.* **33,** 327–349, doi: 10.1007/s11001-013-9166-8.

Donn, W., and M. Blaik (1952). A study and evaluation of the tripartite seismic method of locating hurricane, *Bull. Seismol. Soc. Am.* **43,** 311–329.

Ebeling, C. W. (2012). Inferring ocean storm characteristics from ambient seismic noise: A historical perspective, in *Advances in Geophysics*, R. Dmowska (Editor), Vol. 53, Elsevier, 1–33, doi: 10.1016/b978-0-12-380938-4.00001-x.

Ford, S. R., D. S. Dreger, K. Mayeda, W. R. Walter, L. Malagnini, and W. S. Phillips (2008). Regional attenuation in northern California: A comparison of five 1D Q methods, *Bull. Seismol. Soc. Am.* **98,** 2033–2046, doi: 10.1785/0120070218.

Friedrich, A., F. Krüger, and K. Klinge (1998). Ocean-generated microseismic noise located with the Gräfenberg array, *J. Seismol.* **2,** 47–64, doi: 10.1023/A:1009788904007.

Gal, M., A. M. Reading, S. P. Ellingsen, L. Gualtieri, K. D. Koper, R. Burlacu, H. Tkalčić, and M. A. Hemer (2015). The frequency dependence and locations of short-period microseisms generated in the Southern Ocean and West Pacific, *J. Geophys. Res.* **120,** 5764–5781, doi: 10.1002/2015JB012210.

Gerstoft, P., and T. Tanimoto (2007). A year of microseisms in southern California, *Geophys. Res. Lett.* **34,** L20304, doi: 10.1029/2007GL031091.

Gerstoft, P., M. C. Fehler, and K. G. Sabra (2006). When katrina hit california, *Geophys. Res. Lett.* **33,** L17308, doi: 10.1029/2006GL027270.

Gerstoft, P., P. M. Shearer, N. Harmon, and J. Zhang (2008). Global *P*, *PP*, and *PKP* wave microseisms observed from distant storms, *Geophys. Res. Lett.* **35,** L23306, doi: 10.1029/2008GL036111.

Gilmore, M. H. (1946). Microseisms and ocean storms, *Bull. Seismol. Soc. Am.* **36,** 89–119.

Gualtieri, L., E. Stutzmann, Y. Capdeville, F. Ardhuin, M. Schimmel, A. Mangeney, and A. Morelli (2013). Modelling secondary microseismic noise by normal mode summation, *Geophys. J. Int.* **193,** 1732–1745, doi: 10.1093/gji/ggt090.

Gutenberg, B. (1931). Microseisms in North America, *Bull. Seismol. Soc. Am.* **21,** 1–24.

Hasselmann, K. (1963). A statistical analysis of the generation of microseisms, *Rev. Geophys.* **1,** 177–210, doi: 10.1029/RG001i002p00177.

Haubrich, R. A., and K. McCamy (1969). Microseisms: Coastal and pelagic sources, *Rev. Geophys.* **7,** 539–571, doi: 10.1029/rg007i003p00539.

Hetzer, C. H., K. E. Gilbert, R. Waxler, and C. L. Talmadge (2010). Generation of microbaroms by deep-ocean hurricanes, in *Infrasound Monitoring for Atmospheric Studies*, Springer, Dordrecht, The Netherlands, 249–262.

Hong, T.-K. (2010). *Lg* attenuation in a region with both continental and oceanic environments, *Bull. Seismol. Soc. Am.* **100,** no. 2, 851–858.

Hong, T.-K. (2014). Influence of continental margin on regional seismic wavefield, *Tectonophysics* **627,** 141–158.

Hong, T.-K., and K. Lee (2012). $m_b(Pn)$ scale for the Korean Peninsula and site-dependent *Pn* amplification, *Pure Appl. Geophys.* **169,** no. 11, 1963–1975.

Hong, T.-K., J. Lee, S. Park, H. H. Yoon, W. Kim, and J. S. Shin (2019). Seismic detection of strong ground motions by M_W 5.6 North Korean nuclear explosion, *Sci. Rep.* **91,** 2343–2354.

Jo, E., and T.-K. Hong (2013). V_P/V_S ratios in the upper crust of the southern Korean Peninsula and their correlations with seismic and geophysical properties, *J. Asian Earth Sci.* **66,** 204–214.

Landés, M., F. Hubans, N. M. Shapiro, A. Paul, and M. Campillo (2010). Origin of deep microseisms by using teleseismic body waves, *J. Geophys. Res.* **115,** no. B05302, doi: 10.1029/2009JB006918.

Lee, W. D., B. G. Jo, F. Schwab, and S. B. Jung (2012). Typhoon-generated microseisms observed from the short-period KSRS array, *Geosci. J.* **16,** 447–454, doi: 10.1007/s12303-012-0039-y.

Li, C. F., Z. Zhou, H. Hao, H. Chen, J. Wang, B. Chen, and J. Wu (2008). Late Mesozoic tectonic structure and evolution along the present-day northeastern South China Sea continental margin, *J. Asian Earth Sci.* **31,** 546–561, doi: 10.1016/j.jseaes.2007.09.004.

Li, G., Y. E. Li, H. Zhang, L. Bai, L. Ding, W. Li, Q. Cui, and Y. Zhou (2019). Detection of a thick and weak low-velocity layer atop the mantle transition zone beneath the Northeastern South China Sea from triplicated *P*-wave waveform modeling, *Bull. Seismol. Soc. Am.* **109,** 1181–1193, doi: 10.1785/0120180318.

Longuet-Higgins, M. S. (1950). A theory of the origin of microseisms, *Phil. Trans. Roy. Soc. Lond. A* **243,** 1–35, doi: 10.1098/rsta.1950.0012.

Nishida, K. (2017). Ambient seismic wave field, *Proc. Jpn. Acad. Ser. B* **93,** 423–448, doi: 10.2183/pjab.93.026.

Nishida, K., H. Kawakatsu, Y. Fukao, and K. Obara (2008). Background Love and Rayleigh waves simultaneously generated at the Pacific Ocean floors, *Geophys. Res. Lett.* **35,** L16307, doi: 10.1029/2008GL034753.

Schimmel, M., E. Stutzmann, F. Ardhuin, and J. Gallart (2011). Polarizaed Earth's ambient microseismic noise, *Geochem. Geophys. Geosys.* **12,** no. Q07014, doi: 10.1029/2011GC003661.

Shapiro, N. M., M. H. Ritzwoller, and G. D. Bensen (2006). Source location of the 26 sec microseism from cross-correlations of ambient seismic noise, *Geophys. Res. Lett.* **33,** L18310, doi: 10.1029/2006GL027010.

Stehly, L., M. Campillo, and N. M. Shapiro (2006). A study of the seismic noise from its long-range correlation properties, *J. Geophys. Res.* **111,** no. B10306, doi: 10.1029/2005JB004237.

Stewart, R. H. (2008). *Introduction to Physical Oceanography*, Texas A&M University, College Station, Texas, 345 pp.

Stopa, J. E., K. F. Cheung, M. A. Garcés, and N. Badger (2012). Atmospheric infrasound from nonlinear wave interactions during Hurricanes Felicia and Neki of 2009, *J. Geophys. Res.* **117,** no. C12017, doi: 10.1029/2012JC008257.

Stutzmann, E., M. Schimmel, G. Patau, and A. Maggi (2006). Global climate imprint on seismic noise, *Geochem. Geophys. Geosys.* **10,** no. Q11004, doi: 10.1029/2009GC002619.

Sutton, G. H., and N. Barstow (1990). Ocean-bottom ultralow-frequency (ULF) seismo-acoustic ambient noise: 0.002 to 0.4 Hz, *J. Acoust. Soc. Am.* **87,** 2005–2012, doi: 10.1121/1.399328.

Tabulevich, V. N. (1971). The effect of the velocity of the centre of a cyclone on the generation of microseisms, *Pure Appl. Geophys.* **85,** 69–74, doi: 10.1007/bf00875399.

Tang, Q., and C. Zheng (2013). Crust and upper mantle structure and its tectonic implications in the south China Sea and adjancent regions, *J. Asian Earth Sci.* **62,** 510–525, doi: 10.1016/j.jseaes.2012.10.037.

Tanimoto, T., S. Ishimaru, and C. Alvizuri (2006). Seasonality in particle motion of microseisms, *Geophys. J. Int.* **166,** 253–266.

Tian, Y., and M. H. Ritzwoller (2015). Directionality of ambient noise on the Juan de Fuca plate: Implications for source locations of the primary and secondary microseisms, *Geophys. J. Int.* **201,** 429–443, doi: 10.1093/gji/ggv024.

Tolman, H. L. (1991). A third generation model for wind waves on slowly varying, unsteady and inhomogeneous depth and currents, *J. Phys. Oceanogr.* **21,** 782–797, doi: 10.1175/1520-0485(1991)021<0782:atgmfw>2.0.co;2

Webb, S. C. (1998). Broadband seismology and noise under the ocean, *Rev. Geophys.* **36,** 105–142, doi: 10.1029/97rg02287.

Wu, H. H., Y. B. Tsai, T. Y. Lee, C. H. Lo, C. H. Hsieh, and D. Van Toan (2004). 3-D shear wave velocity structure of the crust and upper mantle in South China Sea and its surrounding regions by surface wave dispersion analysis, *Mar. Geophys. Res.* **25,** 5–27, doi: 10.1007/s11001-005-0730-8.

Yang, Y., and M. H. Ritzwoller (2008). Characteristics of ambient seismic noise as a source for surface wave tomography, *Geochem. Geophys. Geosys.* **9,** no. Q02008, doi: 10.1029/2007GC001814.

Zhang, J., P. Gerstoft, and P. D. Bromirski (2010). Pelagic and coastal sources of *P*-wave microseisms: Generation under tropical cyclones, *Geophys. Res. Lett.* **37,** L15301, doi: 10.1029/2010GL044288.

Manuscript received 15 October 2019
Published online 9 September 2020